Superconductor Science and Technology

Check for updates

PAPER

Microscopic investigation of rf vortex nucleation in Nb_3Sn films using a near-field magnetic microwave microscope

Chung-Yang Wang[1,*], **Zeming Sun**[2], **Thomas Oseroff**[3], **Matthias U Liepe**[2] **and Steven M Anlage**[1]

[1] Quantum Materials Center, Department of Physics, University of Maryland, College Park, MD 20742, United States of America
[2] Department of Physics, Cornell University, Ithaca, NY, United States of America
[*] Author to whom any correspondence should be addressed.

E-mail: chyawang@terpmail.umd.edu

Keywords: superconductor, vortex, SRF, Nb3Sn, microwave, defect

OPEN ACCESS

RECEIVED
18 November 2025

REVISED
21 January 2026

ACCEPTED FOR PUBLICATION
8 February 2026

PUBLISHED
18 February 2026

Original content from this work may be used under the terms of the Creative Commons Attribution 4.0 licence.

Any further distribution of this work must maintain attribution to the author(s) and the title of the work, journal citation and DOI.

Abstract

We use a near-field magnetic microwave microscope to investigate and compare rf vortex nucleation in two superconducting radio-frequency-quality Nb_3Sn films fabricated by different methods: a conventional vapor-diffused film and an electrochemically plated film followed by thermal annealing, both of which are deposited on Nb substrates. The microscope applies a localized rf magnetic field to the sample surface and measures the resulting third-harmonic response P_{3f}, which is particularly sensitive to rf vortex nucleation triggered by surface defects. Both Nb_3Sn films exhibit nontrivial $P_{3f}(T)$ structures below 7 K that display the key signatures associated with rf vortex nucleation at local defects. The electrochemical film additionally shows multiple $P_{3f}(T)$ structures between 14 K and 16 K that are absent in the vapor-diffused sample. Our results highlight the influence of fabrication method on rf vortex penetration properties and demonstrate the utility of third-harmonic response as a local diagnostic tool for surface defects in Nb_3Sn films.

1. Introduction

As a promising material for next-generation superconducting radio-frequency (SRF) cavities [1, 2], Nb_3Sn offers significant performance advantages over conventional niobium. Its high critical temperature ($T_c \approx 18$ K), large superconducting gap, and high superheating field support operation at higher accelerating gradients, offer lower surface resistance, and reduced cryogenic load [3–6]. In particular, the ability to operate SRF cavities near 4 K using compact commercial cryocoolers-rather than complex helium cryomodules-promises to substantially lower system cost and operational complexity [6]. These advantages have driven extensive research into the development of high-quality Nb_3Sn films optimized for SRF performance [4, 7–11].

Despite these advantages, Nb_3Sn films-particularly those fabricated by the conventional vapor diffusion process [6]-face several materials challenges that limit their rf performance. Key issues include excessive surface roughness [12–15], local stoichiometric deviations [16, 17], and impurity incorporation [18], all of which can degrade the superconducting properties and contribute to rf losses [17]. Surface roughness can locally enhance rf magnetic fields, triggering premature vortex entry and quench [12–15]. Stoichiometric inhomogeneities, including both Sn-deficient and Sn-rich regions, introduce spatial variations in T_c, energy gap Δ, and enhance rf dissipation [7, 16, 17, 19]. Grain boundaries are also recognized as potential weak points; recent studies have revealed significant Sn segregation and local suppression of superconductivity at grain boundaries [20], which may act as favorable sites for rf vortex nucleation under strong microwave fields [17].

Overcoming these limitations requires a detailed understanding of local superconducting behavior and the continued development of fabrication methods that improve surface quality. Here, 'surface properties' include both chemical (stoichiometry and impurity levels) and physical (surface roughness, grain shape/size, and grain-boundary geometry and population). The deposition route and its associated phase

© 2026 The Author(s). Published by IOP Publishing Ltd

transformations govern grain growth and the resulting surface properties. For example, electrochemical Sn pre-deposition followed by thermal annealing forms a continuous nucleation seed layer, whereas vapor diffusion relies on adsorption of Sn vapor at initial discrete sites until a nucleation layer coalesces. As a result, electrochemically prepared Nb_3Sn films exhibit improved stoichiometry and reduced roughness ($R_a \approx 60$ nm) compared to typical vapor-diffused films ($R_a \approx 300$ nm), [9, 10] albeit with smaller average grains and more heterogeneous local surface features due to the higher density of nucleation sites. Technologically, vapor diffusion uses comparatively simpler tooling but allows less local control of flux than a pre-deposited Sn layer; electrochemistry enables sufficient local Sn supply but is a specialized process with bath management and operator-dependent variability. These process trade-offs also impact the surface properties, and therefore, nonlinear RF behavior.

As discussed above, rf vortex nucleation arising from surface roughness, stoichiometric inhomogeneity, and Sn segregation at grain boundaries can contribute to losses and limit the rf performance of Nb_3Sn. These mechanisms are inherently local, often originating from nanoscale surface defects that are not easily detected by macroscopic measurement techniques. It is therefore beneficial to adopt a microscopic approach that enables local investigation of rf vortex nucleation due to surface defects. Motivated by this need, we have developed a near-field magnetic microwave microscope [21–35] that applies a localized rf magnetic field to a confined region of the sample and measures the locally-generated third-harmonic response.

The third-harmonic signal P_{3f} is particularly sensitive to rf vortex nucleation: when the applied rf magnetic field exceeds the local vortex penetration field, transient rf semi-loop vortices nucleate and produce a strong nonlinear response at the third harmonic [33, 36]. In a previous study on SRF-quality Nb/Cu films [33], this technique successfully identified surface defects capable of nucleating rf vortices by analyzing the temperature and input power dependence of P_{3f}.

In this work, we apply our near-field magnetic microwave microscope [37, 38] to measure third-harmonic response and investigate rf vortex nucleation in two SRF-quality Nb_3Sn films prepared by different fabrication methods at Cornell University: a traditional vapor-diffused film and an electrochemically plated film followed by thermal annealing [9, 10]. By analyzing the temperature and input power dependence of P_{3f}, we identify nontrivial features consistent with rf vortex nucleation by surface defects. A comparison between the two films provides insight into how surface properties resulting from different fabrication methods influence the nature and distribution of these nonlinear responses.

The structure of this paper is as follows. Section 2 describes the experimental setup of the near-field magnetic microwave microscope used to probe local nonlinear electrodynamics. Section 3 presents the third-harmonic response data obtained from the two Nb_3Sn films, along with a detailed analysis focusing on signatures of surface defects. Section 4 compares the results from both samples and discusses their implications in the context of rf vortex nucleation. Finally, section 5 summarizes the key findings and their relevance to understanding and optimizing Nb_3Sn films for SRF applications.

2. Experimental setup

The experimental setup of the near-field magnetic microwave microscope used in this study is identical to that described in previous works [32–34]. For completeness, a brief overview of the microscope and its operating principles is provided in this section.

The core component of the microwave microscope is a magnetic writer probe, originally designed for conventional hard-disk drives and provided by Seagate Technology. This probe is capable of generating a highly localized and intense rf magnetic field on the surface of the superconductor.

The measurement process begins with the production of a microwave signal $P_{rf}\sin^2(\omega t)$ at frequency $f = \omega/2\pi$ by a microwave source. This signal is transmitted to the magnetic writer probe inside the cryostat via a series of coaxial cables and the built-in transmission line of the probe. The probe then produces a localized rf magnetic field $B_{rf}\sin(\omega t)$, which is applied to the surface of the superconducting sample. In response, the sample generates a time-dependent screening current on and near the surface in an effort to maintain the Meissner state. The magnetic field associated with this screening current is then coupled back to the same probe, creating a return propagating signal on the transmission line. This return signal contains multiple harmonic components, from which the third-harmonic component $P_{3f}\sin^2(3\omega t)$ is isolated using appropriate filtering. The power of this third-harmonic signal is then extracted and measured by a spectrum analyzer at room temperature.

Measurements are performed with a variety of fixed input frequencies ranging from 1.1 GHz to 2.2 GHz, while systematically varying the sample temperature and applied rf field amplitude. The base temperature for a sample in the cryostat is around 3.6 K.

During microwave measurements, the probe is in contact with the sample surface. However, the surfaces of the probe and the sample are not perfectly flat, resulting in a finite probe-sample separation h, which influences both the field of view of the probe and the peak rf magnetic field experienced by the sample B_{pk}. The separation h is estimated to be less than 1 μm, and for an input microwave power of 0 dBm (Here, the rf power in dBm is referenced to 1 mW, i.e. $P_{dBm} = 10\log_{10}\left(\frac{P_{mW}}{1\,mW}\right)$, so 0 dBm = 1 mW.), B_{pk} is estimated to lie within the range of several tens of millitesla [32–35]. The field of view of the probe ranges from sub-micron to micron scale, depending on the probe-sample separation and the specific signal being analyzed [33, 35].

No external DC magnetic field is applied during the measurements. The residual DC field near the sample at low temperatures is measured to be approximately 35 μT using a cryogenic three-axis magnetometer. The corresponding average separation between trapped flux quanta, given by $\sqrt{\Phi_0/B}$, is approximately 7.7 μm, which is significantly larger than the field of view of the microscope probe. Therefore, even if the entire 35 μT residual DC field were to become trapped in the sample, the probability of having a DC vortex directly beneath the probe is low. We note that prior work has examined the microwave flux flow resistivity and depinning frequency of Nb_3Sn bulk material in large DC magnetic fields [39].

Background nonlinear measurements have been performed with the same type of probe in contact with a copper surface as a function of temperature [33]. These measurements show no signs of background nonlinearity arising from the wiring or magnetic properties of the probe for the input power levels used here.

The probe background depends sensitively on the input frequency and varies from probe to probe. For each probe, we therefore select the input frequency to maximize the signal-to-background ratio; consequently, different input frequencies may be used in different measurements. One may ask whether this could affect the interpretation of the P_{3f} results for two reasons: (i) at fixed input power, the rf field amplitude at the sample surface can, in general, depend on frequency, and (ii) superconducting electrodynamic properties are frequency dependent. However, the frequencies used here fall within a relatively narrow band (1.1–2.2 GHz). Moreover, our interpretation relies on qualitative signatures—the temperature and power dependence of P_{3f} features—rather than on absolute P_{3f} magnitudes at a fixed frequency. Accordingly, we do not expect these modest frequency variations to affect the qualitative interpretation.

3. Experimental results

In this work, we investigate two Nb_3Sn films: one deposited using the traditional vapor diffusion process (vapor-diffused Nb_3Sn film) and the other synthesized through an electrochemical plating process followed by thermal annealing (electrochemical Nb_3Sn film). Both films were fabricated at Cornell University. Details on the deposition methods, surface roughness, local stoichiometry, and other characteristics of these films can be found in references [9, 10, 18, 40].

For the measurements on the vapor-diffused Nb_3Sn film, the microscope probe was mounted on a cryogenic *XYZ* positioner and operated in a scanning probe microscope configuration. In contrast, for the measurements on the electrochemical Nb_3Sn film, the probe was fixed in place using a copper clamp and pressed directly against the sample surface to achieve a reduced probe-sample separation. Because the probe-sample separation depends on local surface flatness/contact and is not known with sufficient precision in each measurement, we do not attempt a quantitative comparison of the absolute rf field amplitude between the two films. Instead, we compare qualitative signatures in P_{3f}, in particular the onset temperatures, the presence/absence of defect-related structures, and their temperature- and power-dependence.

3.1. Sample information

Figure 1 shows the two Nb_3Sn films studied: a vapor-diffused film (figure 1(a), nominal 2.0 μm thick) and an electrochemically deposited film (figure 1(b), 2.4 μm thick). Both were prepared on the same grade of high-purity Nb (RRR $\approx$ 300), diced from 3 mm thick plates into 1 cm $\times$ 1 cm coupons. Sn electrodeposition employed a three-electrode system (Pt counter; SCE reference) in an aqueous seed-free $SnCl_2$ / ammonium citrate bath. Sn pre-deposits were converted to Nb_3Sn by high-vacuum annealing (10^{-6} Torr): 500 °C for 5 h (nucleation) followed by 1100 °C for 3 h (alloying), then furnace cooling. Vapor-diffused samples used the same thermal schedule with a separate Sn source providing a controlled Sn-vapor flux at tuned vapor pressure [10].

For the vapor-diffused Nb_3Sn film, third-harmonic response measurements were carried out at a single surface location. For the electrochemical Nb_3Sn film, measurements were performed over multiple sessions, with each session probing a separate surface location. The data presented in the main text

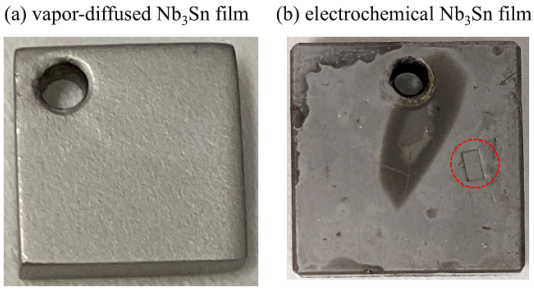

Figure 1. Photographs of the two Nb_3Sn films used in this study, both prepared at Cornell University. (a) Vapor-diffused Nb_3Sn film. (b) Electrochemical Nb_3Sn film. Each sample has lateral dimensions of 1 cm × 1 cm. The red dashed circle in (b) highlights a scar on the surface caused by an aggressive probe contact during a later measurement, which did not affect the data presented in the main text.

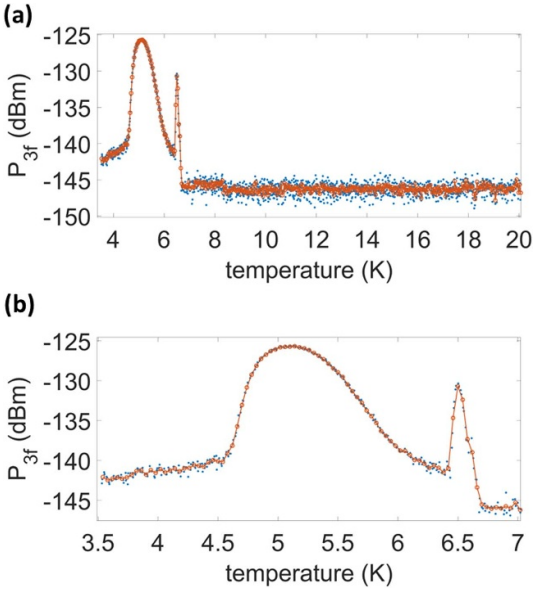

Figure 2. Representative data for P_{3f} as a function of temperature for the vapor-diffused Nb_3Sn film. The input frequency is 2.08 GHz and the input power is −8 dBm. The blue dots are the raw data, and the red curve is the P_{3f} averaged over 0.04 K range bins. (a) Full temperature range from 3.6 K to 20 K. (b) Expanded view of the low-temperature region below 7 K.

were acquired at the first location, prior to any observable surface damage. In a subsequent session, the microscope probe was pressed against the sample with a substantial force, leaving a visible scar on the surface, as indicated by the red dashed circle in figure 1(b). The results obtained after this incident are presented in appendix.

3.2. Experimental results for the vapor-diffused Nb_3Sn film

Figure 2 shows representative third-harmonic response data as a function of temperature, $P_{3f}(T)$, measured at a fixed location on the vapor-diffused Nb_3Sn film. The measurement protocol proceeds as follows: the sample is first warmed to 20 K, above its superconducting transition temperature T_c ($\approx$ 18 K), and then the microwave source is activated with a fixed input frequency ($f = \omega/2\pi = 2.08$ GHz) and input power ($P = -8$ dBm). The third-harmonic response P_{3f} is measured as the sample is gradually cooled down to 3.6 K.

The measured $P_{3f}(T)$ signal in figure 2 contains contributions from both the sample and a temperature-independent background originating from the microscope probe. The magnetic writer probe used as the microscope probe exhibits intrinsic nonlinearity, which remains constant across temperature. This probe background dominates the signal above 18 K. A significant increase in P_{3f} is observed below 6.7 K, as shown in figure 2(b). We define this onset temperature of strong third-harmonic generation as the P_{3f} transition temperature, denoted $T_c^{P_{3f}}$. The emergence of enhanced nonlinearity below $T_c^{P_{3f}}$ indicates the presence of additional mechanisms-likely extrinsic in origin-associated with material capable of generating strong nonlinear microwave response.

Table 1. The four key features of $P_{3f}(T)$ due to rf semi-loop vortex nucleation associated with surface defects.

Feature 1	$P_{3f}(T)$ onsets below T_c of Nb_3Sn and shows a bell-shaped structure.
Feature 2	$P_{3f}(T)$ maximum increases for a stronger driving rf field amplitude.
Feature 3	$P_{3f}(T)$ maximum shows up at a lower temperature for a stronger driving rf field amplitude.
Feature 4	$P_{3f}(T)$ low-temperature onset shows up at a lower temperature for a stronger driving rf field amplitude.

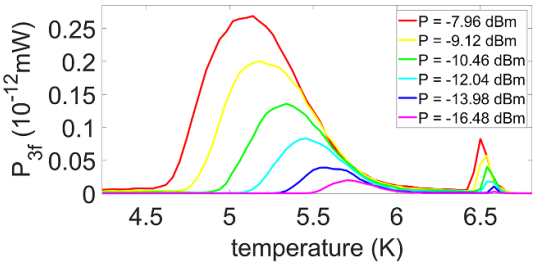

Figure 3. Measured $P_{3f}(T)$ on a linear power scale for the vapor-diffused Nb_3Sn film at an input frequency of 2.08 GHz, with input power decreasing from strong (red) to weak (purple). Compared to the raw data shown in figure 2, here the probe background is subtracted. The input power levels are not evenly spaced in power but rather in rf field amplitude. Note that the input power is proportional to the square of the rf field amplitude.

One may notice that the intrinsic Nb_3Sn response near its bulk superconducting transition around 18 K is absent in figure 2. This is because our local P_{3f} measurements are primarily sensitive to surface defects, rather than the intrinsic nonlinear response of the superconductor [33]. Since the primary objective of this work is to investigate the rf properties of surface defects, the strong third-harmonic response observed below 6.7 K, as shown in figure 2, forms the central focus of the following analysis.

As presented in previous work [33], the microwave microscope can locally nucleate rf semi-loop vortices [41] at surface defects beneath the probe, producing a third-harmonic response $P_{3f}(T)$ that exhibits four characteristic features. In that study, time-dependent Ginzburg–Landau (TDGL) simulations were also performed using a phenomenological grain boundary toy model, where grain boundaries were modeled as regions containing low-T_c impurity phases. Notably, both the experimental measurements and the TDGL simulations revealed the same four robust features in $P_{3f}(T)$, indicative of rf semi-loop vortex nucleation at grain boundaries. These four features are summarized in table 1 and serve as diagnostic criteria in the following analysis for identifying defect-induced rf semi-loop vortex nucleation in the Nb_3Sn films.

To further investigate the nature of the third-harmonic response of the vapor-diffused Nb_3Sn film below 6.7 K, as shown in figure 2, $P_{3f}(T)$ measurements are performed at a series of input powers P, corresponding to different applied rf field amplitudes. For each measurement, the sample is first warmed to 20 K and then gradually cooled to 3.6 K while subjected to a fixed-frequency rf field (2.08 GHz) at a constant input power. To isolate the sample response, the probe background is estimated by averaging the $P_{3f}(T)$ magnitude between 19 K and 20 K and is subtracted from the total signal. This procedure is repeated for six different input powers. The resulting background-subtracted $P_{3f}(T)$ curves at a fixed location on the vapor-diffused Nb_3Sn film are shown on a linear power scale in figure 3. The input power levels are chosen to span uniform steps in rf field amplitude, rather than in power. Note that the input power is proportional to the square of the rf field amplitude.

Two distinct nontrivial structures are observed in figure 3, corresponding to $P_{3f}(T)$ onsets (upon cooling) at $T_c^{P_{3f}} = 6.2$ K and $T_c^{P_{3f}} = 6.7$ K, respectively. The presence of two separate $T_c^{P_{3f}}$ values suggests that the measured $P_{3f}(T)$ is the superposition of two defect signals. Both $P_{3f}(T)$ structures exhibit the four key characteristics outlined in table 1, indicating that they both likely originate from rf semi-loop vortex nucleation associated with surface defects. These results indicate that the vapor-diffused Nb_3Sn film contains at least two distinct surface defects, each capable of nucleating rf vortices but with different associated P_{3f} transition temperatures due to local variation in superconducting properties.

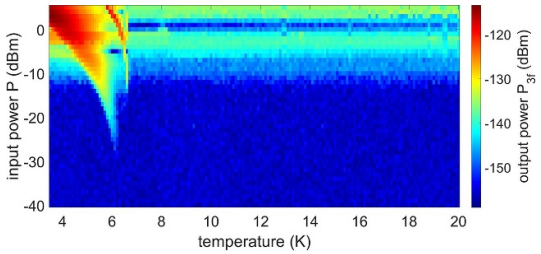

Figure 4. Color map of the measured third-harmonic power P_{3f} (in dBm, log scale) as a function of temperature T and input power P for the vapor-diffused Nb_3Sn film. The input frequency is 2.08 GHz. The input-power-dependent probe background is not subtracted.

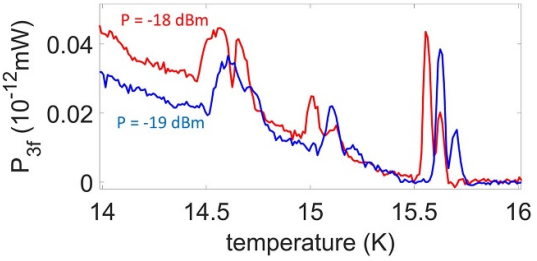

Figure 5. Measured linear power scale $P_{3f}(T)$ for the electrochemical Nb_3Sn film at an input frequency of 1.21 GHz. Data are shown for two different input powers: $P = -18$ dBm (red) and $P = -19$ dBm (blue). The probe background has been subtracted.

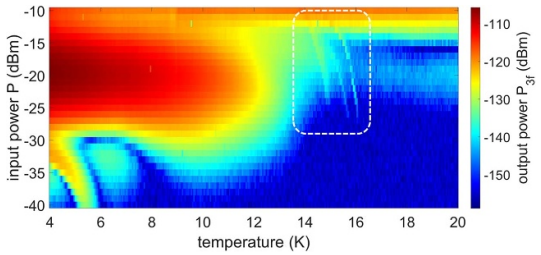

Figure 6. Color map of the measured log power scale P_{3f} as a function of temperature T and input power P for the electrochemical Nb_3Sn film. The input frequency is 1.21 GHz. The input-power-dependent probe background is not subtracted. The white dashed box highlights the region containing the three nontrivial $P_{3f}(T)$ structures, whose details are shown in figure 5.

To complement the $P_{3f}(T)$ measurements performed over a limited input power range, we also conducted a broader input power sweep, as shown in figure 4. This measurement spans temperatures from 3.6 K to 20 K, exceeding the intrinsic T_c of Nb_3Sn, and input powers from -40 dBm to $+5$ dBm. Across this expanded parameter space, no additional nontrivial $P_{3f}(T)$ structures are observed beyond the two features previously identified in figure 3.

3.3. Experimental results for the electrochemical Nb_3Sn film

The temperature and input power dependence of P_{3f} in the electrochemical Nb_3Sn film are studied using the same measurement protocol as for the vapor-diffused film. Figure 5 shows the third-harmonic response $P_{3f}(T)$ on a linear power scale, measured at a fixed location on the electrochemical Nb_3Sn film for two different input powers. The input frequency is 1.21 GHz, and the probe background has been subtracted from the data. While $P_{3f}(T)$ is recorded over the full temperature range from 20 K to 3.6 K, figure 5 highlights the nontrivial $P_{3f}(T)$ structures that emerge between 14 K and 16 K.

Three distinct nontrivial $P_{3f}(T)$ structures are observed in figure 5: one around 15.6 K, another around 15.1 K, and a third around 14.6 K. Each of these $P_{3f}(T)$ structures exhibits the four key features outlined in table 1, indicating that they are likely associated with rf vortex nucleation by surface defects. The presence of multiple P_{3f} transitions at different temperatures suggests that the electrochemical Nb_3Sn film contains several surface defects with varying local superconducting properties.

In addition to the $P_{3f}(T)$ measurements over a limited input power range, we also perform a broader scan across both temperature and input power, as shown in figure 6. This figure presents the measured third-harmonic power P_{3f} (in dBm, color scale) as a function of temperature T (horizontal axis) and input power P (vertical axis) for the electrochemical Nb_3Sn film. The input frequency is 1.21 GHz, and the input-power-dependent probe background is not subtracted. The measurement spans temperatures from 4 K to 20 K, and input powers from −40 dBm to −10 dBm. This extended color map enables a comprehensive view of the nonlinear response landscape and highlights the emergence of power-sensitive features.

As described by the four key features in table 1, nontrivial $P_{3f}(T)$ structures arising from rf vortex nucleation by surface defects tend to shift to lower temperatures as the rf field amplitude increases. In a P_{3f} color map such as figure 6, where temperature is plotted on the horizontal axis and input power on the vertical axis, this behavior manifests as a structure with a negative slope.

The white dashed box in figure 6 highlights the region containing the three nontrivial P_{3f} structures observed between 14 K and 16 K, which are shown in greater detail in figure 5. In addition to these three structures, another distinct P_{3f} structure appears in the lower-left corner of figure 6, within the range $-40\,\text{dBm} < P < -30\,\text{dBm}$ and $4\,\text{K} < T < 6\,\text{K}$. This P_{3f} structure, indicated by the orange and yellow region, has a transition temperature $T_c^{P_{3f}}$ near 6 K and exhibits a pronounced negative slope. Such negative slope behavior is consistent with the characteristic signatures of rf semi-loop vortex nucleation by surface defects. Taken together, all four P_{3f} structures display the key features outlined in table 1, supporting their interpretation as nonlinear responses originating from localized rf vortex nucleation at defect sites.

Compared to the lower-left P_{3f} structure, the three P_{3f} structures observed between 14 K and 16 K appear only at significantly higher input powers. This indicates that the corresponding rf vortices nucleate under stronger rf field amplitudes, suggesting higher local vortex penetration thresholds at those defect sites. Such behavior may result from one of two scenarios: (1) the defects possess intrinsically higher local vortex penetration fields, or (2) the defects are located deeper beneath the surface, or at some lateral distance from the probe, requiring stronger rf fields to activate their nonlinear response.

The strongest P_{3f} signal in figure 6, represented by the large red region below 12 K, has a very weak negative slope trend. This behavior suggests that it may originate from a nonlinear mechanism distinct from rf semi-loop vortex nucleation at grain boundaries. At this point, we do not have a definitive microscopic explanation of this feature.

4. Discussion

Both Nb_3Sn films studied in this work-the vapor-diffused (see figures 3 and 4) and electrochemical (see figure 6) samples-exhibit nontrivial third-harmonic response structures below 7 K. These $P_{3f}(T)$ structures occur well below the intrinsic superconducting transition temperature of stoichiometric Nb_3Sn ($T_c \approx 18\,\text{K}$) and consistently display the four key characteristics associated with rf vortex nucleation by surface defects, as outlined in table 1. The observation of similar P_{3f} structures in both films, despite their different deposition methods and surface properties, suggests that they likely share comparable types of surface defects capable of nucleating rf vortices.

It is known that a number of second phases can exist in Nb_3Sn films. For example two other superconducting inter-metallic compounds exist in the Nb–Sn system, and have reported transition temperatures of $T_c = 2.68\,\text{K}$ ($NbSn_2$) and $T_c = 2.07\,\text{K}$ (Nb_6Sn_5), [42] both well below our measurement temperature range. Some Nb_3Sn films are known to have residual Sn droplets on the surface [43, 44]. In some vapor-diffused Nb_3Sn samples, a surface Sn layer overlies the native oxides, giving a local cross-sectional sequence of Sn / oxides / Nb_3Sn / Nb [45]. However, the superconducting transition temperature of pure Sn is known to be $T_c = 3.72\,\text{K}$ [46], just at the lower edge of our measurement range. It should be noted that no evidence of a transition near the T_c of the Nb substrates is seen in either film.

On the other hand, the two Nb_3Sn films do exhibit notable differences in the number, temperature distribution, and power thresholds of the observed P_{3f} structures that are likely associated with rf vortex nucleation by surface defects. The vapor-diffused film displays two distinct P_{3f} structures, both appearing below 7 K, whereas the electrochemical film exhibits four such structures-one below 6 K and three between 14 K and 16 K. In contrast, no nontrivial P_{3f} structures are observed above 7 K in the vapor-diffused film. The three P_{3f} structures between 14 K and 16 K in the electrochemical film appear only at relatively high rf field amplitudes. At lower rf power levels-for example, $P = -30\,\text{dBm}$-these defects likely do not nucleate rf vortices in our local measurements.

The observation of P_{3f} structures with $T_c^{P_{3f}}$ below the intrinsic T_c of stoichiometric Nb_3Sn (≈18 K) suggests that certain surface regions of the films exhibit degraded superconducting properties. A likely

origin of this behavior is local non-stoichiometry, particularly Sn deficiency, which is known to significantly suppress T_c [9, 10, 47–50]. Notably, T_c drops to approximately 7 (5) K for Sn concentrations near 18 (14) % [47], consistent with the P_{3f} transition temperatures observed in this work. In vapor-diffused Nb_3Sn, spatially nonuniform Sn vapor supply during growth can result in Sn-deficient grains and stoichiometric inhomogeneity near the surface. It is also known that the vapor-diffused Nb_3Sn growing from the Nb interface often suffers from Sn deficiency, and the film thickness can vary considerably over the sample (for example, see the cross-section Sn composition images in figure 6 of [10]). Although the electrochemical synthesis method improves average stoichiometric uniformity, isolated Sn-deficient regions have also been reported near the surface [10]. These Sn-deficient regions likely give rise to the observed low-temperature P_{3f} structures at 6.5 K and below in both films. It has also been calculated that strongly overdoped A15 Nb–Sn films will show transition temperatures as low as 5 K at 31% Sn [50].

5. Conclusion

In this work, we use our near-field magnetic microwave microscope to study rf vortex nucleation in two SRF-quality Nb_3Sn films prepared by different fabrication methods, linking the response to surface properties. Both the vapor-diffused and electrochemical films exhibit nontrivial third-harmonic response structures below 7 K. The observation of similar low-temperature nonlinear features in both films suggests that they likely share comparable types of surface defects, despite differences in their growth techniques. In addition, the electrochemical film displays additional P_{3f} structures between 14 K and 16 K that are absent in the vapor-diffused film, indicating variations in the distribution or characteristics of these defects. These results suggest that fabrication methods can influence not only surface roughness and stoichiometry, but also the rf vortex penetration landscape. This measurement technique provides a useful diagnostic tool for identifying surface defects and guiding the optimization of Nb_3Sn films for SRF applications.

Data availability statement

The data that support the findings of this study are openly available at the following URL/DOI: http://hdl.handle.net/1903/34 791 [51].

Acknowledgments

The authors would like to thank Javier Guzman from Seagate Technology for providing magnetic write probes, and Nathan Sitaraman for helpful discussions. This work is funded by the U S Department of Energy/High Energy Physics through Grant No. DESC0017931, the Army Research Office under Grant Number ARO W911NF-24-1-0153, and the Maryland Quantum Materials Center.

Appendix. Additional data collected after surface damage to the electrochemical Nb_3Sn Film

This appendix presents P_{3f} measurements performed on the electrochemical Nb_3Sn film after the creation of a visible surface scar, caused by unintentional mechanical contact and deformation with the microscope probe (see figure 1(b)). These measurements were collected during a later experimental session and are not included in the main analysis. They are presented here to highlight the distinct nonlinear response that emerged following the damage.

Figure 7 shows the third-harmonic response $P_{3f}(T)$ measured on the electrochemical Nb_3Sn film after surface damage. The measurement was performed at an input frequency of 1.84 GHz and an input power of −14 dBm, with the probe background subtracted. A notable enhancement in P_{3f} is observed below 9.8 K. The inset highlights an oscillatory structure in $P_{3f}(T)$ between 6.8 K and 7.8 K, which is not present in the pre-damage measurements (see figures 5 and 6). This feature may reflect modified local electrodynamic properties introduced by the surface scar.

The oscillatory behavior is also evident in the rf field amplitude dependence. Figure 8 presents $\sqrt{P_{3f}}$ as a function of $\sqrt{P}$ at five temperatures ranging from 6.7 K to 8.5 K. The measurements were taken at an input frequency of 1.84 GHz, with the probe background subtracted. Since $\sqrt{P}$ is proportional to the applied rf magnetic field amplitude, these curves reflect the nonlinear response to increasing rf field amplitude. Pronounced oscillations in $\sqrt{P_{3f}}$ are observed across all temperatures, with the effect

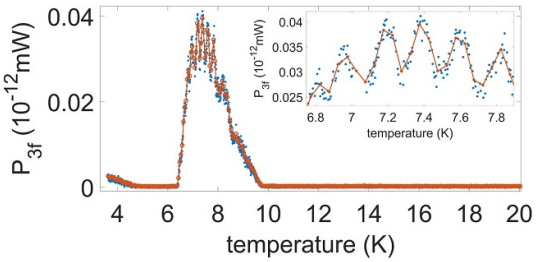

Figure 7. Third-harmonic response P_{3f} as a function of temperature for the electrochemical Nb_3Sn film after surface damage. The input frequency is 1.84 GHz and the input power is −14 dBm. The probe background has been subtracted. The inset shows a magnified view of the $P_{3f}(T)$ structure between 6.8 K and 7.8 K.

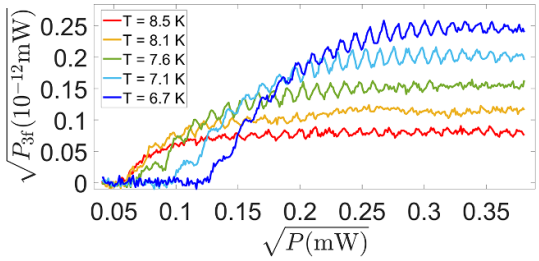

Figure 8. Third-harmonic response $\sqrt{P_{3f}}$ as a function of the square root of input power $\sqrt{P}$ at five different temperatures for the electrochemical Nb_3Sn film after surface damage. The measurement was performed at a fixed input frequency of 1.84 GHz, and the probe background has been subtracted. Note that $\sqrt{P}$ is proportional to the applied rf magnetic field amplitude.

becoming more pronounced as temperature decreases. The oscillations in $\sqrt{P_{3f}}$ are approximately periodic as a function of $\sqrt{P}$ on a linear scale. For reference, an input power of $P = -14$ dBm corresponds to $\sqrt{P(\mathrm{mW})} = 0.2$.

The oscillatory patterns observed in $P_{3f}(T)$ and $P_{3f}(\sqrt{P})$ (figures 7 and 8, respectively) are absent in the pre-damage measurements (figures 5 and 6) and are likely associated with changes to the surface introduced by the scar. Similar oscillatory behavior has been reported in a previous study of SRF-grade Nb samples [32], where it was attributed to the rf response of weak-link Josephson junctions. In the present case, it is possible that pressing the microscope probe against the electrochemical Nb_3Sn film with a substantial force modified the film surface and locally formed weak-link regions beneath the microscope probe, which could explain the emergence of the oscillatory patterns in the third-harmonic response. These results demonstrate the sensitivity of third-harmonic measurements to local surface conditions and highlight their potential as a diagnostic for identifying weak-link behavior induced by mechanical or structural imperfections.

ORCID iDs

Chung-Yang Wang 0000-0001-8429-9633
Zeming Sun 0000-0001-5816-5578
Thomas Oseroff 0000-0003-3888-1678

References

[1] Padamsee H 2017 50 years of success for SRF accelerators-a review *Supercond. Sci. Technol.* **30** 053003
[2] Anlage S M 2021 Microwave superconductivity *IEEE J. Microw.* **1** 389–402
[3] Kneisel P, Kupfer H, Schwarz W, Stoltz O and Halbritter J 1977 On properties of superconducting Nb_3Sn used as coatings in RF cavities *IEEE Trans. Magn.* **13** 496–9
[4] Posen S, Liepe M and Hall D L 2015 Proof-of-principle demonstration of Nb_3Sn superconducting radiofrequency cavities for high Q applications *Appl. Phys. Lett.* **106** 082601
[5] Posen S, Valles N and Liepe M 2015 Radio frequency magnetic field limits of Nb and Nb_3Sn *Phys. Rev. Lett.* **115** 047001
[6] Posen S and Hall D L 2017 Nb_3Sn superconducting radiofrequency cavities: fabrication, results, properties and prospects *Supercond. Sci. Technol.* **30** 033004
[7] Becker C, Posen S, Groll N, Cook R, Schlepütz C M, Hall D L, Liepe M, Pellin M, Zasadzinski J and Proslier T 2015 Analysis of Nb_3Sn surface layers for superconducting radio frequency cavity applications *Appl. Phys. Lett.* **106** 082602

[8] Ilyina E A, Rosaz G, Descarrega J B, Vollenberg W, Lunt A J G, Leaux F, Calatroni S, Venturini-Delsolaro W and Taborelli M 2019 Development of sputtered Nb_3Sn films on copper substrates for superconducting radiofrequency applications *Supercond. Sci. Technol.* **32** 035002

[9] Sun Z *et al* 2021 Toward stoichiometric and low-surface-roughness Nb_3Sn thin films via direct electrochemical deposition *Proc. SRF'21* pp 516–21

[10] Sun Z, Baraissov Z, Porter R D, Shpani L, Shao Y-T, Oseroff T, Thompson M O, Muller D A and Liepe M U 2023 Smooth, homogeneous, high-purity Nb_3Sn superconducting RF resonant cavity by seed-free electrochemical synthesis *Supercond. Sci. Technol.* **36** 115003

[11] Howard K, Liepe M U and Sun Z 2023 Thermal annealing of DC sputtered Nb_3Sn and V_3Si thin films for superconducting radiofrequency cavities *J. Appl. Phys.* **134** 225301

[12] Porter R, Hall D L, Liepe M and Maniscalco J T 2016 Surface roughness effect on the performance of Nb_3Sn cavities *28th Linear Accel. Conf. (LINAC 2016)* vol 16 pp 129–32 (available at: https://accelconf.web.cern.ch/linac2016/papers/moprc027.pdf)

[13] Porter R D, Hu H, Liepe M, Stilin N A, Sun Z and Tao M J 2019 Progress in Nb_3Sn SRF cavities at cornell university *North Am. Part. Acc. Conf.* **19** 37

[14] Posen S, Lee J, Seidman D N, Romanenko A, Tennis B, Melnychuk O S and Sergatskov D A 2021 Advances in Nb_3Sn superconducting radiofrequency cavities towards first practical accelerator applications *Supercond. Sci. Technol.* **34** 025007

[15] Pack A R, Carlson J, Wadsworth S and Transtrum M K 2020 Vortex nucleation in superconductors within time-dependent Ginzburg-Landau theory in two and three dimensions: role of surface defects and material inhomogeneities *Phys. Rev. B* **101** 144504

[16] Trenikhina Y, Posen S, Romanenko A, Sardela M, Zuo J M, Hall D L and Liepe M 2017 Performance-defining properties of Nb_3Sn coating in SRF cavities *Supercond. Sci. Technol.* **31** 015004

[17] Carlson J *et al* 2021 Analysis of magnetic vortex dissipation in Sn-segregated boundaries in Nb_3Sn superconducting RF cavities *Phys. Rev. B* **103** 024516

[18] Sun Z, Baraissov Z, Dukes C A, Dare D K, Oseroff T, Thompson M O, Muller D A and Liepe M U 2023 Surface oxides, carbides and impurities on RF superconducting Nb and Nb_3Sn: a comprehensive analysis *Supercond. Sci. Technol.* **36** 115030

[19] Lee J, Posen S, Mao Z, Trenikhina Y, He K, Hall D L, Liepe M and Seidman D N 2019 Atomic-scale analyses of Nb_3Sn on Nb prepared by vapor diffusion for superconducting radiofrequency cavity applications: a correlative study *Supercond. Sci. Technol.* **32** 024001

[20] Lee J *et al* 2020 Grain-boundary structure and segregation in Nb_3Sn coatings on Nb for high-performance superconducting radiofrequency cavity applications *Acta Mater.* **188** 155–65

[21] Lee S-C, Vlahacos C P, Feenstra B J, Schwartz A, Steinhauer D E, Wellstood F C and Anlage S M 2000 Magnetic permeability imaging of metals with a scanning near-field microwave microscope *Appl. Phys. Lett.* **77** 4404–6

[22] Lee S-C and Anlage S M 2003 Study of local nonlinear properties using a near-field microwave microscope *IEEE Trans. Appl. Supercond.* **13** 3594–7

[23] Lee S-C and Anlage S M 2003 Spatially-resolved nonlinearity measurements of $YBa_2Cu_3O_{7-\delta}$ bicrystal grain boundaries *Appl. Phys. Lett.* **82** 1893–5

[24] Lee S-C, Sullivan M, Ruchti G R, Anlage S M, Palmer B S, Maiorov B and Osquiguil E 2005 Doping-dependent nonlinear Meissner effect and spontaneous currents in high-T_c superconductors *Phys. Rev. B* **71** 014507

[25] Lee S-C, Lee S-Y and Anlage S M 2005 Microwave nonlinearities of an isolated long $YBa_2Cu_3O_{7-\delta}$ bicrystal grain boundary *Phys. Rev. B* **72** 024527

[26] Mircea D I, Xu H and Anlage S M 2009 Phase-sensitive harmonic measurements of microwave nonlinearities in cuprate thin films *Phys. Rev. B* **80** 144505

[27] Tai T, Xi X X, Zhuang C G, Mircea D I and Anlage S M 2011 Nonlinear near-field microwave microscope for RF defect localization in superconductors *IEEE Trans. Appl. Supercond.* **21** 2615–8

[28] Tai T, Ghamsari B G and Anlage S M 2012 Nanoscale electrodynamic response of Nb superconductors *IEEE Trans. Appl. Supercond.* **23** 7100104

[29] Tai T, Ghamsari B G and Anlage S M 2014 Modeling the nanoscale linear response of superconducting thin films measured by a scanning probe microwave microscope *J. Appl. Phys.* **115** 203908

[30] Tai T, Ghamsari B G, Bieler T R, Tan T, Xi X X and Anlage S M 2014 Near-field microwave magnetic nanoscopy of superconducting radio frequency cavity materials *Appl. Phys. Lett.* **104** 232603

[31] Tai T, Ghamsari B G, Bieler T and Anlage S M 2015 Nanoscale nonlinear radio frequency properties of bulk Nb: origins of extrinsic nonlinear effects *Phys. Rev. B* **92** 134513

[32] Oripov B *et al* 2019 High-frequency nonlinear response of superconducting cavity-grade Nb surfaces *Phys. Rev. Appl.* **11** 064030

[33] Wang C-Y, Pereira C, Leith S, Rosaz G and Anlage S M 2024 Microscopic examination of rf-cavity-quality niobium films through local nonlinear microwave response *Phys. Rev. Appl.* **22** 054010

[34] Wang C-Y and Anlage S M 2024 Near-field nonlinear microwave microscope for fundamental superconducting studies *2024 IEEE/MTT-S Int. Microwave Symp. - IMS 2024* pp 998–1001

[35] Wang C-Y and Anlage S M 2025 Microwave microscope studies of trapped vortex dynamics in superconductors *Phys. Rev. B* **111** 214524

[36] Oripov B and Anlage S M 2020 Time-dependent Ginzburg-Landau treatment of rf magnetic vortices in superconductors: vortex semiloops in a spatially nonuniform magnetic field *Phys. Rev. E* **101** 033306

[37] Anlage S M, Steinhauer D E, Feenstra B J, Vlahacos C P and Wellstood F C 2001 Near-field microwave microscopy of materials properties *Microwave Superconductivity* ed H Weinstock and M Nisenoff (Springer) 239–69

[38] Anlage S M, Talanov V V and Schwartz A R 2007 Principles of near-field microwave microscopy *Scanning Probe Microscopy: Electrical and Electromechanical Phenomena at the Nanoscale* vol 1, ed S V Kalinin and A Gruverman (Springer) pp 215–53

[39] Alimenti A, Pompeo N, Torokhtii K, Spina T, Flükiger R, Muzzi L and Silva E 2021 Microwave measurements of the high magnetic field vortex motion pinning parameters in Nb_3Sn *Supercond. Sci. Technol.* **34** 014003

[40] Sun Z, Dare D K, Baraissov Z, Muller D A, Thompson M O and Liepe M U 2023 Thermodynamic route of Nb_3Sn nucleation: role of oxygen *APL Mater.* **11** 071118

[41] Gurevich A and Ciovati G 2008 Dynamics of vortex penetration, jumpwise instabilities and nonlinear surface resistance of type-II superconductors in strong rf fields *Phys. Rev. B* **77** 104501

[42] Charlesworth J P 1966 The superconducting transition temperatures of Nb_6Sn_5 and $NbSn_2$ *Phys. Lett.* **21** 501–2

[43] Sayeed Md N, Pudasaini U, Reece C E, Eremeev G and Elsayed-Ali H E 2019 Structural and superconducting properties of Nb_3Sn films grown by multilayer sequential magnetron sputtering *J. Alloys Compd.* **800** 272–8
[44] Jiang G *et al* 2024 Understanding and optimization of the coating process of the radio-frequency Nb_3Sn thin film superconducting cavities using tin vapor diffusion method *Appl. Surf. Sci.* **643** 158708
[45] Baraissov Z, Sun Z, Liepe M and Muller D 2024 Improving chemical composition measurements from microscale to atomic scale with fused multi-modal microscopy *Microsc. Microanal.* **30** ozae044.114
[46] Corak W S and Satterthwaite C B 1956 Atomic heats of normal and superconducting tin between 1.2° and 4.5 °K *Phys. Rev.* **102** 662–6
[47] Moore D F, Zubeck R B, Rowell J M and Beasley M R 1979 Energy gaps of the A-15 superconductors Nb_3Sn, V_3Si and Nb_3Ge measured by tunneling *Phys. Rev. B* **20** 2721
[48] Devantay H, Jorda J L, Decroux M, Muller J and Flükiger R 1981 The physical and structural properties of superconducting A15-type Nb-Sn alloys *J. Mater. Sci.* **16** 2145–53
[49] Li Y and Gao Y 2017 GLAG theory for superconducting property variations with A15 composition in Nb_3Sn wires *Sci. Rep.* **7** 1133
[50] Sitaraman N S, Kelley M M, Porter R D, Liepe M U, Arias T A, Carlson J, Pack A R, Transtrum M K and Sundararaman R 2021 Effect of the density of states at the Fermi level on defect free energies and superconductivity: a case study of Nb_3Sn *Phys. Rev. B* **103** 115106
[51] Wang C Y 2025 Dataset for Figures in Microscopic Investigation of rf Vortex Nucleation in Nb3Sn Films Using a Near-Field Magnetic Microwave Microscope *Digital Repository at the University of Maryland* (available at: http://hdl.handle.net/1903/34791)